

Alma Mater Studiorum Università di Bologna
Archivio istituzionale della ricerca

Nickel-Mediated Enantioselective Photoredox Allylation of Aldehydes with Visible Light

This is the final peer-reviewed author's accepted manuscript (postprint) of the following publication:

Published Version:

Calogero, F., Potenti, S., Bassan, E., Fermi, A., Gualandi, A., Monaldi, J., et al. (2022). Nickel-Mediated Enantioselective Photoredox Allylation of Aldehydes with Visible Light. *ANGEWANDTE CHEMIE. INTERNATIONAL EDITION*, 61(11), e202114981-e202114981 [10.1002/anie.202114981].

Availability:

This version is available at: <https://hdl.handle.net/11585/881706> since: 2023-02-03

Published:

DOI: <http://doi.org/10.1002/anie.202114981>

Terms of use:

Some rights reserved. The terms and conditions for the reuse of this version of the manuscript are specified in the publishing policy. For all terms of use and more information see the publisher's website.

This item was downloaded from IRIS Università di Bologna (<https://cris.unibo.it/>).
When citing, please refer to the published version.

(Article begins on next page)

This is the final peer-reviewed accepted manuscript of:

Nickel-Mediated Enantioselective Photoredox Allylation of Aldehydes with Visible Light

F. Calogero, S. Potenti, E. Bassan, A. Fermi, A. Gualandi, J. Monaldi, B. Dereli, B. Maity, L. Cavallo, P. Ceroni, and P. G. Cozzi

Angew. Chem.Int. Ed. 2022, 61, e2021149

DOI: 10.1002/anie.202114981

The final published version is available online at:

<https://onlinelibrary.wiley.com/doi/pdf/10.1002/anie.202114981>

This item was downloaded from IRIS Università di Bologna
(<https://cris.unibo.it/>)

When citing, please refer to the published version

Nickel-Mediated Enantioselective Photoredox Allylation of Aldehydes with Visible Light

Francesco Calogero, Simone Potenti, Elena Bassan, Andrea Fermi, Andrea Gualandi,*
Jacopo Monaldi, Busra Dereli, Bholanath Maity, Luigi Cavallo,* Paola Ceroni,* and
Pier Giorgio Cozzi*

Abstract: Here we report a practical, highly enantioselective photoredox allylation of aldehydes mediated by chiral nickel complexes with commercially available allyl acetate as the allylating agent. The methodology allows the clean stereoselective allylation of aldehydes in good to excellent yields and up to 93 % e.e. using a catalytic amount of $\text{NiCl}_2(\text{glyme})$ in the presence of the chiral aminoindanol-derived bis(oxazoline) as the chiral ligand. The photoredox system is constituted by the organic dye 3DPAFIPN and a Hantzsch's ester as the sacrificial reductant. The reaction proceeds under visible-light irradiation (blue LEDs, 456 nm) at 8–12 °C. Compared to other published procedures, no metal reductants (such as Zn or Mn), additives (e.g. CuI) or air-sensitive $\text{Ni}(\text{COD})_2$ are necessary for this reaction. Accurate DFT calculations and photophysical experiments have clarified the mechanistic picture of this stereoselective allylation reaction.

Introduction

Allylation of carbonyls is a key strategy for the preparation of functionalized building blocks in the total synthesis of natural products.^[1] Allylation or propargylation^[2] reactions with organometallic reagents are well established and employed methodologies to access homo-allylic or homo-propargylic alcohols and amines. In particular, enantioselective allylation methodologies were applied to solve practical synthetic problems and were scaled-up to access to valuable

starting materials. In this kind of classical addition to carbonyl, prevalently based on the use of organometallic reagents or on metal-catalyzed reductive C–C couplings, the use of stoichiometric amounts of metals (organometallic reagents or metallic reductants) is predominant.^[3] The advent of photoredox catalysis has enabled the employment of a different effective strategy (Figure 1).

Photoredox catalysis combines the use of a photocatalyst (metal complex, organic dye or semiconductor) with light for the formation of radical species by photoinduced electron transfer (PET).^[4] Metallaphotoredox catalysis, i.e. metal catalysis merged with photoredox catalysis, is a new and rapidly growing research area.^[5] By using metallaphotoredox catalysis, it is possible to access nucleophilic organometallic reagents.^[6] A suitable C-centered radical, formed under photoredox conditions, is converted into an organometallic nucleophile^[7] through its capture with a suitable transition metal.^[8] New interesting methods based on chromium,^[9] titanium,^[10] cobalt,^[11] and bismuth^[12] were recently published.^[8,13] As an example of translation of classical organometallic chemistry into a photoredox mediated methodology, the well-known Nozaki–Hiyama–Kishi (NHK) reaction, which is relevant in total synthesis,^[14] was reported by Glorius^[9a–d] and Kanai^[9e–g] in a light-driven fashion. In their photocatalytic methods, photogenerated allyl radicals are trapped by the catalytic Cr^{II} leading to the formation of a transient nucleophilic Cr^{III} allyl reagent. By photoredox catalysis, it was also possible to restore the Cr^{II} reagent via reduction of the intermediate Cr^{III} species, replacing the stoichiometric reducing Mn in the protocol for the NHK reactions reported by Fürstner and co-workers.^[15] An enantioselective photoredox version of the reaction was also investigated by the same authors,^[9c,e,f] 20 years after the development of the first stereoselective protocol.^[16] Unfortunately, it was not possible to extend these noteworthy results to the synthesis of unsubstituted homoallylic alcohols.

Even though these approaches are innovative and reliable, there is room for improvements. On the one hand, several effective enantioselective methodologies, with different nucleophilic allylating reagents (i.e. allylic stannanes,^[17] allylic halides,^[18] allylic acetates,^[19] and allylic boronates^[20]), have been reported. However, such useful and important protocols shown some drawbacks and limitations. Thanks to the enhanced stability to moisture and air, allyl silanes could represent the solution to overcome the above-mentioned drawbacks,^[21] nevertheless, their low nucleophilicity still

[*] F. Calogero, S. Potenti, E. Bassan, Dr. A. Fermi, Dr. A. Gualandi, J. Monaldi, Prof. P. Ceroni, Prof. P. G. Cozzi
Dipartimento di Chimica “Giacomo Ciamician”
Alma Mater Studiorum—Università di Bologna
Via Selmi 2, 40126, Bologna (Italy)
E-mail: andrea.gualandi10@unibo.it
paola.ceroni@unibo.it
piergiorgio.cozzi@unibo.it

S. Potenti
Laboratorio SMART
Scuola Normale Superiore
Piazza dei Cavalieri 7, 56126, Pisa (Italy)
B. Dereli, Dr. B. Maity, Prof. L. Cavallo
KAUST Catalysis Center (KCC), Division of Physical Sciences and Engineering
King Abdullah University of Science and Technology (KAUST)
Thuwal 23955 (Saudi Arabia)
E-mail: luigi.cavallo@kaust.edu.sa

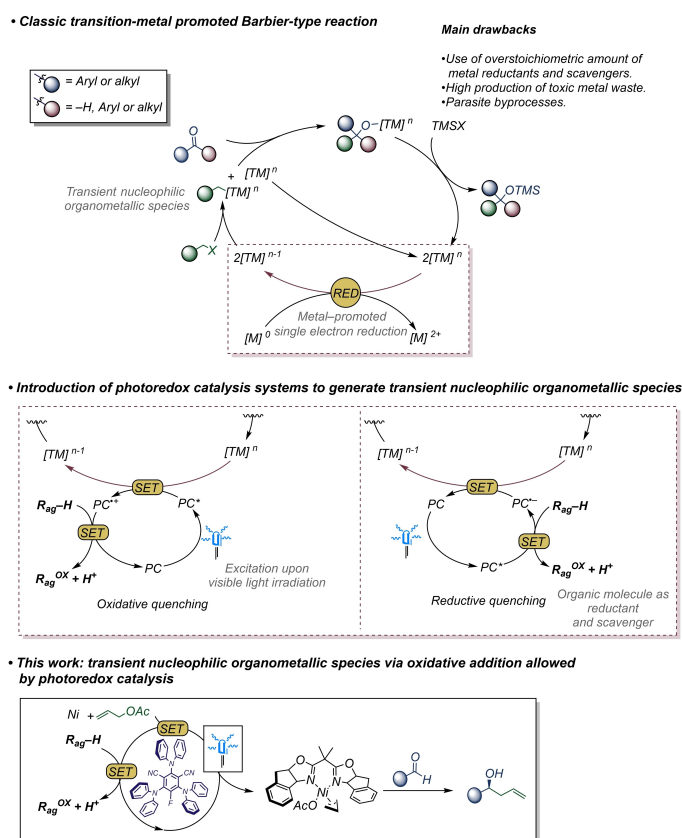


Figure 1. Photoredox synergistic allylations of aldehydes.

represents the main limitation for their application.^[22] Quite recently, we have reported a nickel photoredox allylation of aldehydes with allylacetates.^[23] Aiming to develop a stereoselective variant of the reaction,^[24] we faced many problems due to the scarce reactivity and low enantioselectivity in the selected reaction conditions (aldehyde 1 equiv., DIPEA 3 equiv., allylacetate 3 equiv., [Ru(bpy)₃]Cl₂ 1 mol %, NiCl₂-(glyme) 10 mol %, Bn(BOX) **L6** 20 mol %, blue LED r.t.; 50 % yield, 42 % e.e.).^[23] We have performed comprehensive investigations by varying conditions and photocatalyst, ending up with an effective new protocol that employs the commercially available or easily synthesizable 3DPAFIPN (2,4,6-tris(diphenylamino)-5-fluoroisophthalonitrile) as the photocatalyst^[25] and Hantzsch's ester^[26] as the sacrificial reductant. We are now presenting a valid, reproducible, enantioselective photoredox allylation of aldehydes based on the use of a bench-stable nickel complex and a simply prepared IndaBOX chiral ligand **L1**.^[27] Furthermore, DFT calculations allowed us to shed light on the catalytic cycle, thus presenting mechanistic insights that could be relevant for further studies.

Results and Discussion

After a long unsuccessful journey encompassing an extensive examination of many chiral ligands (see Supporting Information for some selected ligands considered) in our

previous nickel-mediated photoredox allylation reaction,^[23] we hypothesized that a major drawback in the reaction was the presence of a large excess of *N,N*-diisopropylethylamine (DIPEA) as sacrificial reductant. In fact, its ability to coordinate nickel^[28] hampers an effective and stereoselective catalytic cycle. Moreover, we decided to move from [Ru(bpy)₃]Cl₂ to more reducing photocatalysts, selecting organic cyanoarene-based dyes. These dyes display Thermally Activated Delayed Fluorescence (TADF)^[29] and, on the basis of our experience, give successful results in other metal mediated photoredox processes.^[25d] Additionally, in the mentioned photoredox processes, the presence of Hantzsch's ester (HE) was also crucial for the allylation reaction performed with titanium,^[10] cobalt,^[11b] and bismuth.^[12]

The role played by the HE in these new conditions was found to be quite unique, since a series of different sacrificial reductants (see Supporting Information for details) were found less suitable for the reaction. The key role played by HE in this and, probably, in other metallaphotoredox catalytic cycles, is important and quite peculiar, as will be evidenced and discussed in the section of the paper dedicated to DFT investigations. Table 1 shows some salient points about our optimization studies. We were able to control the enantioselectivity of the model reaction, performing the reaction in THF, in 0.4 M aldehyde concentration. Light and nickel are both necessary for the success of the enantioselective transformation (Table 1, entries 4 and 5). A careful control of the reaction temperature (see Supporting Information for pictures and description) was necessary to enhance the enantioselectivity of the reaction. We found that elimination of water traces (3 Å MS) was also crucial to improve enantioselectivity.^[30] The most compelling chiral ligand **L1** was prepared in large scale with the Reisman's reported methodology,^[27] while other BOX ligands were found to give reduced enantioselectivity. (Table 1, entries 7–13). TADF photocatalysts performed better compared to Ru^{II} or Ir^{III} metal-based photocatalysts (Table 1, entries 1 and 22 vs. entries 23 and 24). Although the enantioselective reaction can be carried out in other solvents (Table 1, entries 18–21), slightly better results were obtained in THF. A major e.e. was obtained in toluene but a lower conversion was observed (Table 1, entry 18).

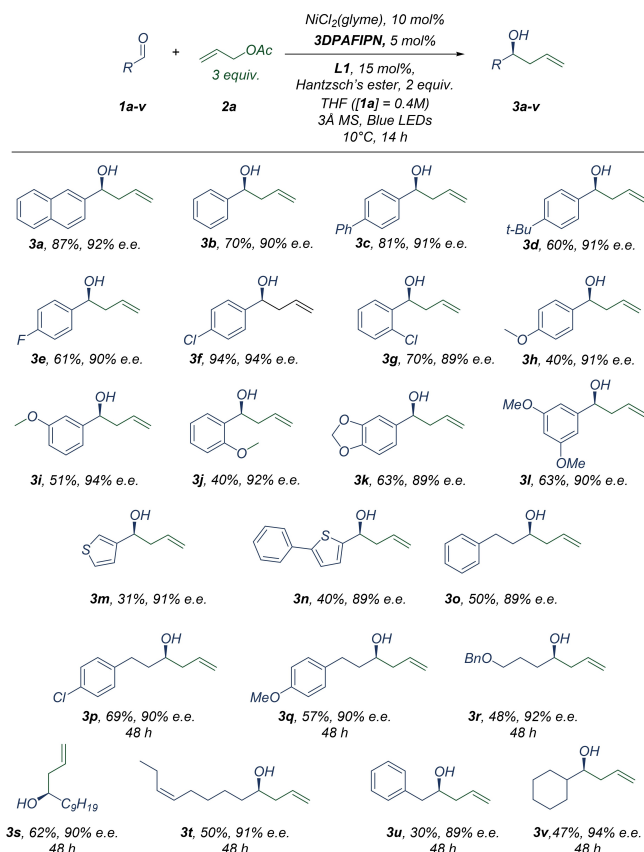
The selected reaction conditions were employed with aromatic and aliphatic aldehydes (Scheme 1). The absolute configuration of the homoallylic alcohols, isolated after purification, was established in the case of **3a**^[31] and **3o**^[32] by comparison with the data reported in literature. For all the substrates studied the allylating agent attacks the prochiral *Si* face of carbonyl group. Electron-rich (**1h–l**) or electron-poor (**1e–g**) aromatic aldehydes are suitable substrates for our enantioselective allylation protocol. The *ortho* or *para* substituents seem to influence neither reactivity nor stereoselectivity of this nickel mediated allylation. Heterocyclic substrates are tolerated in certain cases (**1m,n**). Unsuccessful results were observed for some aldehydes (see Supporting Information), due either to the chelation ability of the heteroatom (e.g., unsubstituted thiophene 2-carboxaldehyde), or to the limited stability of the products (e.g., *N*-Boc

Table 1: Allylation reaction and variations of some reaction parameters.

Entry	Deviations from standard conditions	Yield [%] ^[b]	e.e. ^[c]
1	none	> 99 (87) ^[d]	92
2	no photocatalyst, with irradiation at 456 nm	0	—
3	allyl bromide instead of allyl acetate	traces	—
4	no nickel	0	—
5	no light	0	—
6	10 mol % of L1	90	90
7 ^[e,f]	L2 instead of L1	70	71
8 ^[e]	L3 instead of L1	> 99	67
9 ^[e]	L4 instead of L1	33	0
10 ^[e,f]	L5 instead of L1	25	3
11 ^[e,f]	L6 instead of L1	98	67
12 ^[e]	L7 instead of L1	93	0
13 ^[e]	L8 instead of L1	traces	—
14 ^[e,g]	[1a] = 0.05 M	91	25
15 ^[e,g]	[1a] = 0.1 M	45	70
16 ^[e,g]	[1a] = 0.2 M	98	79
17	[1a] = 0.2 M	> 99	90
18	toluene instead of THF	30	93
19	MeCN instead of THF	90	85
20	DME instead of THF	22	91
21	DMF instead of THF	88	50
22	4CzIPN instead of 3DPAFIPN	88	89
23 ^[h]	{Ir[dF(CF ₃)ppy] ₂ (dtbbpy)} (PF ₆) instead of 3DPAFIPN	51	88
24 ^[i]	[Ru(bpy) ₃]Cl ₂ ·6 H ₂ O instead of 3DPAFIPN	25	—
25	[Ru(bpy) ₃]Cl ₂ ·6 H ₂ O instead of 3DPAFIPN	traces	25

[a] Reactions performed on 0.1 mmol scale. [b] Determined by ¹H NMR analysis. [c] Determined by HPLC analysis on chiral column. [d] Reaction performed on 0.2 mmol scale. The value in parenthesis is the isolated yield (chromatographic purification). [e] Reaction performed in absence of molecular sieves. [f] [1a] = 0.1 M. [g] Reaction was carried out using 10 mol % of chiral ligand. [h] 1% of the photocatalyst was used. [i] Based on our previous work, reaction was carried out using 3 equiv. of DIPEA as reducing agent and 0.5 mL of MeCN as solvent.

indolyl and pyrrolyl carbaldehyde) in the presence of the pyridinium ion derived by oxidation of HE, acting as a Brønsted acid.^[10] Regarding aliphatic aldehydes, while cyclohexyl aldehyde (**1v**) is a reactive substrate, pivalic



Scheme 1. Photoredox enantioselective nickel-promoted allylations of aldehydes.

aldehyde was not reactive (see Supporting Information for details). Better results are obtained with linear and substituted long chain aliphatic aldehydes (**1o–u**), and the desired products were isolated with moderate yields but with e.e.s ranging from 89 % to 94 %. **3DPAFIPN** is quite stable in the reaction conditions as we have verified, by means of internal standard experiments involving ¹⁹F NMR, determining the amount of the catalyst present in the reaction mixture at the end of the reaction. The photophysical studies and, in particular, Stern–Volmer analysis carried out on the full reaction mixture, revealed important features in our reaction.

3DPAFIPN was chosen as the photocatalyst because of its photophysical and redox properties.^[25] In deaerated, stabilizer-free THF solution, it shows an absorption band in the visible region ($\epsilon = 14900 \text{ M}^{-1} \text{ cm}^{-1}$ at $\lambda = 370 \text{ nm}$; abs onset at 470 nm in THF, Figure S6) and an emission band peaked at 520 nm due to prompt fluorescence ($\tau = 3.6 \text{ ns}$) and delayed fluorescence ($\tau = 110 \mu\text{s}$). The photophysical investigation was therefore aimed at studying the interaction between **3DPAFIPN** and the species present in the reaction mixture. Unexpectedly, upon addition of 20 μM Hantzsch's ester (**HE**) the delayed fluorescence of **3DPAFIPN** shows a biexponential emission decay of 18 and 110 μs : upon increasing the concentration of **HE** up to 130 μM , the biexponential decays can be fitted by the same lifetime components, but the shorter component has an increasing

contribution at the expense of the longer component (Figure S10). The short-lifetime component has been attributed to a static quenching with the association between the photocatalyst and **HE** at the ground state to form a complex, namely **3DPAFIPN·HE**. Under the experimental conditions used to perform the reaction, the formation of this complex is considered quantitative in view of the large excess of **HE** present in the reaction mixture. Therefore, we can consider the complex **3DPAFIPN·HE** as the photoredox active species (see Figure 2). We then analyzed quenching processes of this species by the different components of the reaction mixture (see Supporting Information for more details). No significant lifetime change was observed upon addition of allyl acetate or naphthaldehyde, indicating that no bimolecular quenching processes occur between the complex and these two substrates. On the contrary, upon further addition of **HE** (concentration higher than 130 μM), a dynamic quenching of the emission of the **3DPAFIPN·HE** complex is observed (Figure S15, $k_q = 2.11 \times 10^8 \text{ M}^{-1} \text{ s}^{-1}$).

Quenching has been observed also in the presence of **NiCl₂L1** with $k_q = 5.49 \times 10^8 \text{ M}^{-1} \text{ s}^{-1}$ (Figure S14). Given the higher concentration of **HE** in the reaction conditions compared to that of **NiCl₂L1** (see Supporting Information for the determination of solubilities), the quenching efficiency is higher for the former (79 %) compared to the latter (21 %) and the first single electron transfer (SET) that takes place leads to the reductive quenching of the lowest excited state of the **3DPAFIPN·HE** complex.

We also used photophysical measurements to evaluate the association constant for the formation of the chiral nickel complex upon mixing **NiCl₂(glyme)** and the chiral ligand: the estimated association constant is 44700 M^{-1} (see Supporting Information), a value that ensures a quantitative formation of the **NiCl₂L1** in the reaction conditions.

To shed further light on the reaction mechanism and explore the origin of enantioselectivity, we have performed density functional theory (DFT) calculations (see Computational Details in Supporting Information). In the DFT study, we have selected **1a** and **2a** as the reactants, and **L1** as the Ni^{II} ligand. The complete mechanism is divided into two main sections corresponding to the photoredox catalytic cycle (Figure 3) and to the nickel catalytic cycle (Figure 4).

Photoredox Catalytic Cycle

The photophysical study described above indicated that the initial formation of a **3DPAFIPN·HE** complex is responsible for photoredox catalytic reactivity, so we performed the DFT calculations considering this complex reacting along the reductive or oxidative cycles. These two photoredox catalytic cycles (Figure 3) start with the same step, which is the photoinduced excitation of **3DPAFIPN·HE** to the singlet excited state (Figure S16 and S17), eventually transformed into triplet $^3\text{3DPAFIPN·HE}$ by ISC (intersystem crossing). Along the reductive cycle $^3\text{3DPAFIPN·HE}$ (or the singlet excited state $^*\text{3DPAFIPN·HE}$ in equilibrium with it) is reduced to **3DPAFIPN·HE^{•−}** by oxidation of **HE** to **HE^{•+}** (SET1), and the so-formed **3DPAFIPN·HE^{•−}** is then oxidized to **3DPAFIPN·HE** by the reduction of $^1\text{Ni}^{\text{II}}$ to $^2\text{Ni}^{\text{I}}$ (SET2). The calculated 1e^- reduction potential of the $^3\text{3DPAFIPN·HE}/\text{3DPAFIPN·HE}^{\bullet-}$ pair is lower than that of the **HE^{•+}/HE** indicating the SET1 is thermodynamically less favored (Table 2). Differently, SET2 is highly favored because of the lower 1e^- reduction potential of the **3DPAFIPN·HE}/\text{3DPAFIPN·HE}^{\bullet-} pair than that of the $^1\text{Ni}^{\text{II}}/2\text{Ni}^{\text{I}}$ pair.**

Along the oxidative cycle $^3\text{3DPAFIPN·HE}$ is oxidized to **3DPAFIPN·HE^{•+}** by the reduction of $^1\text{Ni}^{\text{II}}$ to $^2\text{Ni}^{\text{I}}$ (SET3), and the so formed **3DPAFIPN·HE^{•+}** is then reduced to **3DPAFIPN·HE** by the oxidation of **HE** to **HE^{•+}** (SET4). SET3 is thermodynamically favored as the calculated 1e^- reduction potential of the $^1\text{Ni}^{\text{II}}/2\text{Ni}^{\text{I}}$ pair is higher than that of **3DPAFIPN·HE^{•+}}/\text{3DPAFIPN·HE}**, while SET4 is unfavored as the 1e^- reduction potential of the **3DPAFIPN·HE^{•+}}/\text{3DPAFIPN·HE}** pair is lower than that of **HE^{•+}/HE** pair (Table 2).

In accordance with the calculated 1e^- reduction potentials, both the oxidative cycle and reductive cycle are characterized by one exergonic SET step and one endergonic SET with lower activation barriers (Table S9 in Supporting Information). Therefore, consistently with the above photophysical experimental study, the DFT analysis suggests that both cycles are possible, with the experimental preference for the reductive quenching explained by the higher concentration of the **HE** (see Figure 2 and related discussion).

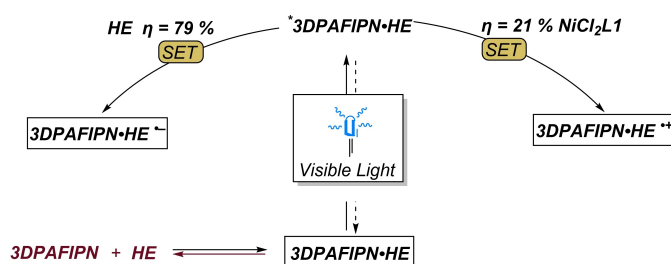


Figure 2. Schematic picture of the photocatalytic mechanism.

Table 2: Calculated reduction potentials, $E_{1/2}^{\text{red}}$ in V, of the most relevant species involved in the catalytic cycles shown in Figure 3 and Scheme S3. The potentials are reported against the saturated calomel electrode (SCE) at 298.15 K in acetonitrile solvent.

Half Reaction	$E_{1/2}^{\text{red}}$ [V]
$^3\text{3DPAFIPN·HE} + 1\text{e}^- \rightarrow \text{3DPAFIPN·HE}^{\bullet-}$	0.58
$\text{3DPAFIPN·HE} + 1\text{e}^- \rightarrow \text{3DPAFIPN·HE}^{\bullet-}$	−1.63
$\text{3DPAFIPN·HE}^{\bullet+} + 1\text{e}^- \rightarrow ^3\text{3DPAFIPN·HE}$	−1.38
$\text{3DPAFIPN·HE}^{\bullet+} + 1\text{e}^- \rightarrow \text{3DPAFIPN·HE}$	0.83
$\text{HE}^{\bullet+} + 1\text{e}^- \rightarrow \text{HE}$	0.93
$^1\text{Ni}^{\text{II}} + \text{HE}^{\bullet+} + 1\text{e}^- \rightarrow ^2\text{Ni}^{\text{I}} + \text{HE}^{\bullet+}/\text{Cl}^-$	−0.58
$^2\text{Ni}^{\text{I}} + \text{HE}^{\bullet+} + 2\text{a} + 1\text{e}^- \rightarrow ^3\text{Ni}^{\text{0}} + \text{HE}^{\bullet+}/\text{Cl}^-$	−1.46

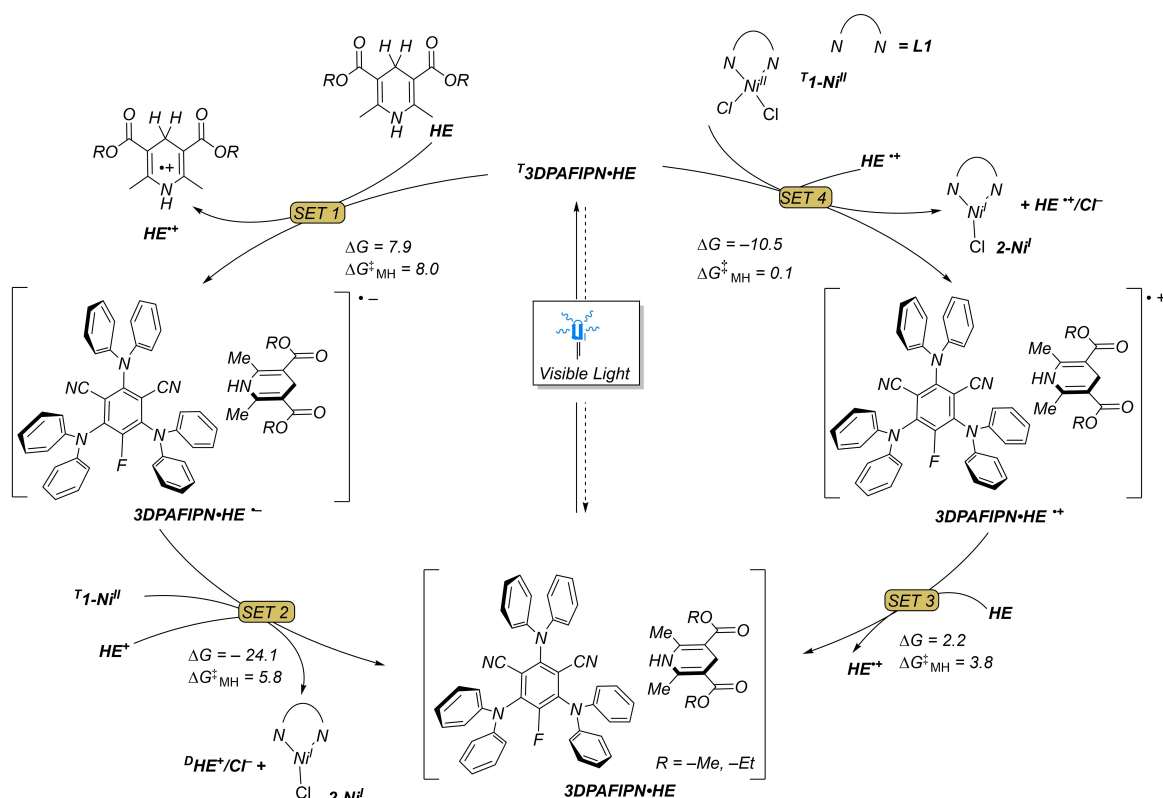


Figure 3. Two alternative mechanisms for the photoredox catalytic cycle. Free energy values at the M06(SMD-THF)/Def2-TZVPP/SDD//PBE(SMD-THF)/Def2-SVP/SDD level of theory are presented. ΔG_{MH}^{\ddagger} have been approximated using Marcus–Hush theory (see Supporting Information for details).

Nickel Catalytic Cycle

As discussed before, the nickel precatalyst $^11-Ni^{II}$ is reduced to $2-Ni^I$, which can be considered as an active nickel catalyst.^[33] However, the first step, corresponding to oxidative addition of **2a** to $2-Ni^I$, requires a very high activation barrier of $41.9 \text{ kcal mol}^{-1}$ (Scheme S2), indicating that $2-Ni^I$ is catalytically inactive for the studied reaction. Nevertheless, similarly to $^11-Ni^{II}/2-Ni^I$ discussed above (SET2), $2-Ni^I$ can be reduced to $3-Ni^0$ by $3DPAFIPN-HE^{\bullet-}$ within the photoredox catalytic cycle. The details of the Ni^I/Ni^0 reduction are discussed in the Supporting Information (Scheme S3). For the Ni^0 species, we explored different ligand variations (Figure S18), and we found $3-Ni^0$ reported in Figure 4 as the most stable. Therefore, we investigated nickel catalytic cycle starting with $3-Ni^0$ as the active catalyst (Figure 4). The energy profile and the mechanism of formation of the desired *S*-product are shown in Figure 4, while the geometries of the transition states leading to the two enantiomers are reported in Figure S19. Focusing on Figure 4, the nickel catalytic cycle starts with the oxidative addition of coordinated **2a** to the nickel atom of $3-Ni^0$ via transition state $[3-4]^{\ddagger}$ and an energy barrier of $16.0 \text{ kcal mol}^{-1}$, leading to $^14-Ni^{II}$. The moderate barrier along with high the exergonicity ($-12.1 \text{ kcal mol}^{-1}$) indicates that this oxidative addition step is facile. The resulting Ni^{II} -intermediate $^14-Ni^{II}$ undergoes exergonic $1e^-$ reduction

coupled with $3DPAFIPN-HE^{\bullet-}/3DPAFIPN-HE$ oxidation to generate the Ni^I -intermediate $5-Ni^I$, through SET7 in Figure 4. The latter is a highly exergonic process, with a ΔG of $-19.9 \text{ kcal mol}^{-1}$. The reaction continues with the insertion of the carbonyl group of **1a** into the Ni-allyl bond in $5-Ni^I$ via transition state $[5-6]_S^{\ddagger}$ and an energy barrier of $11.9 \text{ kcal mol}^{-1}$, leading to 6_S-Ni^I . This corresponds to the enantioselective step, with formation of the stereogenic center. As an alternative, we tried to interchange the sequence of SET and C=O insertion steps (pink line in Figure 4). Along this pathway insertion of the carbonyl group of **1a** into the Ni-allyl bond in $^14-Ni^{II}$, via transition state $^1[4-9]_S^{\ddagger}$ and an energy barrier of $12.5 \text{ kcal mol}^{-1}$, leads to $^19_S-Ni^{II}$, from which one electron reduction, i.e. SET8, leads to the common intermediate 6_S-Ni^I . However, this alternative pathway is energetically disfavored, and was not considered further. Back to the favored pathway (blue line in Figure 4), the next step is the hydrogen atom transfer (HAT) from the radical species of $HE^{\bullet+}/AcO^-$ to 6_S-Ni^I , which occurs via formation of the stable complex of $^17_S-Ni^I$, a step exergonic by $5.6 \text{ kcal mol}^{-1}$. The HAT occurs via transition state $^1[7-8]_S^{\ddagger}$ and a free energy barrier of $16.9 \text{ kcal mol}^{-1}$, leading to 8_S-Ni^0 with the liberation of **HP** (Hantzsch pyridine) and acetic acid. The desired product, already formed in the 8_S-Ni^0 intermediate, is replaced by another molecule of **2a** to regenerate the $3-Ni^0$.

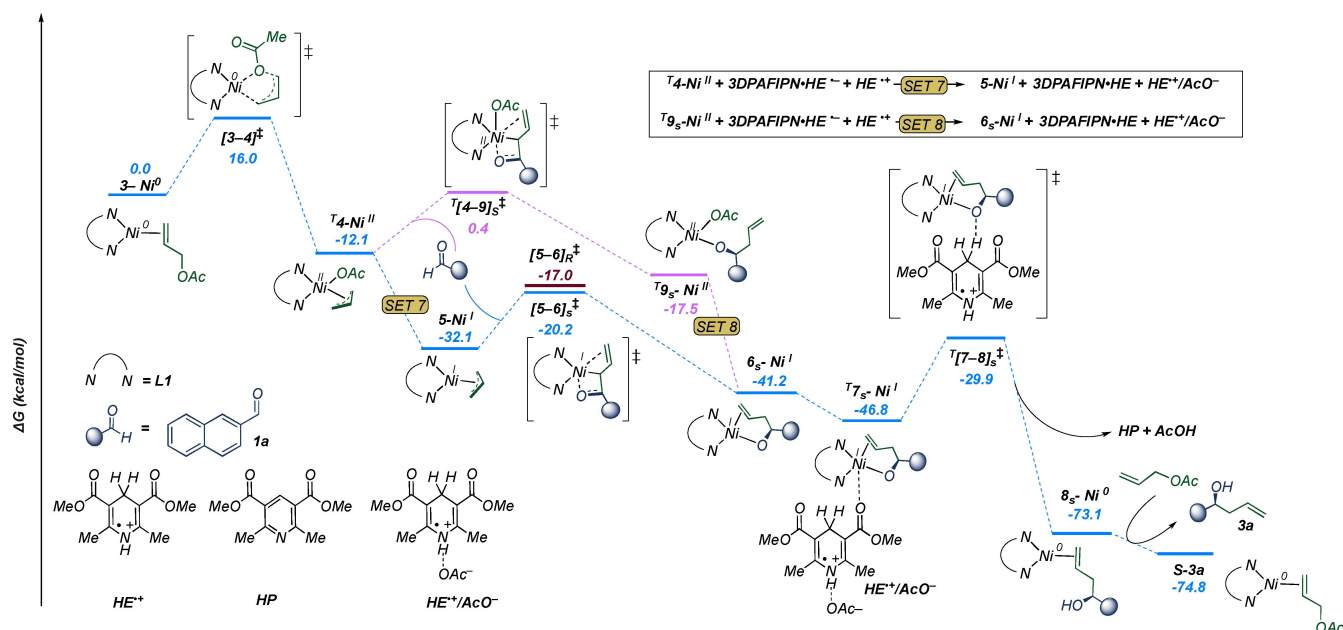


Figure 4. Proposed mechanism for the nickel catalytic cycle of allylation of aldehydes. For energy conventions, refer to Figure 3.

Origin of Enantioselectivity

Having clarified the overall mechanism leading to formation of the experimentally favored *S*-product, we focused on the enantioselective steps from **5-Ni^I** to **6_S-Ni^I**, leading to the formation of the *S*-product (Figure 4). Calculations indicate that transition state **[5-6]_S[‡]**, leading to the *S*-product, is favored by 3.2 kcal mol⁻¹ over transition state **[5-6]_R[‡]**, leading to the *R*-product, which is in agreement with the experimentally observed high enantioselectivity favoring formation of the *S*-product. Inspection of the competing transition state geometries (Figure 5) indicates that the **L1** ligand shapes a chiral catalytic pocket^[34] with hindered north-west (NW) and south-east (SE) quadrants, and unhindered north-east (NE) and south-west quadrants (SW) quadrants. In the favored **[5-6]_S[‡]** transition state the reacting substrates are placed in the unhindered SW and NE quadrants, minimizing steric interaction with the **L1** ligand. In contrast, the substrate is placed in the more hindered NW and SE quadrants in transition state **[5-6]_R[‡]**, with the **L1** ligand bending away from the substrate, as evidenced by a flattening of the bumps in NW and SE quadrants (note the greenish color of the bumps in **[5-6]_R[‡]**, compared to the orange bumps in **[5-6]_S[‡]**). This steric clash between the substrate and the **L1** ligand explains the higher energy of in **[5-6]_R[‡]**.

Conclusion

In summary, we have reported a highly enantioselective methodology based on dual nickel and photoredox catalysis for the stereoselective allylation of aldehydes. The role of **3DPAFIPN** was thoroughly analyzed and carefully interpreted from the photophysical point of view, allowing to

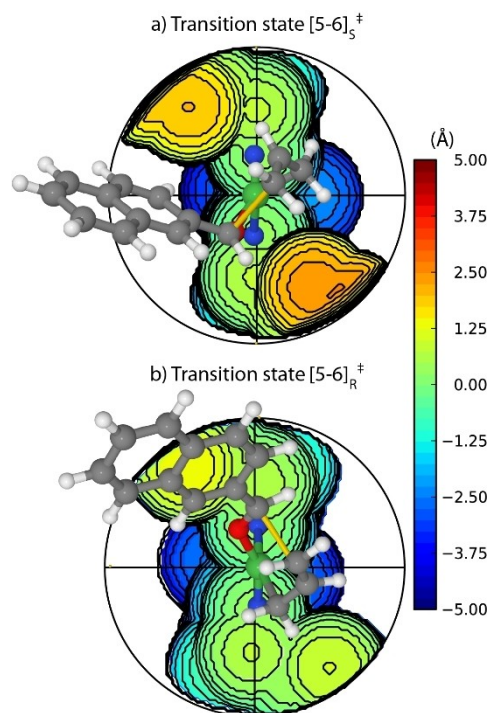


Figure 5. Optimized geometries of transition states pro-*S*, i.e. **[5-6]_S[‡]** (a), and pro-*R*, i.e. **[5-6]_R[‡]** (b), with the Ni atom, the N atom of the **L1** ligand and the substrates represented as ball-and-stick, overlapped to the steric map of the **L1** ligand. The emerging C-C bond is colored in gold.

draw a mechanistic picture of the reaction which is additionally supported by theoretical calculations. A distinctive mechanism for the turnover of the nickel catalyst is suggested, adding a new feature to the multifaceted

reactivity of the Hantzsch's ester. This novel photoredox-mediated enantioselective allylation is based on an easily synthesized chiral ligand and Ni^{II} species, and avoids the manipulation of air-sensitive Ni⁰ in a glovebox. An inexpensive cooling apparatus guarantees the control of temperature necessary for obtaining e.e.s from 89 % to 94 %. Further studies—aiming to extend this protocol to ketones and to exploit other redox-active metals for enantioselective photoredox reactions—are in progress and will be reported in due time.

Acknowledgements

P.G.C. acknowledges National project (PRIN 2017 ID: 20174SYJAF) SURSUMCAT “Raising up Catalysis for Innovative Developments” for financial support of this research. L.C. acknowledges King Abdullah University of Science and Technology (KAUST) for support within the CRG8 program, project the URF/1/4025-01-01, and the KAUST Supercomputing Laboratory for providing computational resources on the Shaheen II HPC infrastructure, and A.G., P.G.C. and P.C. acknowledge the University of Bologna for financial support.

Conflict of Interest

The authors declare no conflict of interest.

Data Availability Statement

The data that support the findings of this study are available from the corresponding author upon reasonable request.

Keywords: Aldehydes · Allylation · Enantioselectivity · Nickel · Photoredox Catalysis

- [1] For selected reviews, see: a) M. Yus, J. C. Gonzalez-Gomez, F. Foubelo, *Chem. Rev.* **2013**, *113*, 5595–5698; b) K. Spielmann, G. Niel, R. M. de Figueiredo, J.-M. Campagne, *Chem. Soc. Rev.* **2018**, *47*, 1159–1173; c) L. Süssé, B. M. Stoltz, *Chem. Rev.* **2021**, *121*, 4084–4099; d) M. Holmes, L. A. Schwartz, M. J. Krische, *Chem. Rev.* **2018**, *118*, 6026–6052.
- [2] C.-H. Ding, X.-L. Hou, *Chem. Rev.* **2011**, *111*, 1914–1937.
- [3] a) A. Gansäuer, H. Blum, *Chem. Rev.* **2000**, *100*, 2771–2788; b) A. Fürstner, *Chem. Rev.* **1999**, *99*, 991–1046.
- [4] For a key contribution: D. Nicewicz, D. W. C. MacMillan, *Science* **2008**, *322*, 77–80. For selected reviews on photoredox catalysis, see: a) T. P. Yoon, M. A. Ischay, J. Du, *Nat. Chem.* **2010**, *2*, 527–532; b) J. M. R. Narayanan, C. R. J. Stephenson, *Chem. Soc. Rev.* **2011**, *40*, 102–113; c) J. Xuan, W.-J. Xiao, *Angew. Chem. Int. Ed.* **2012**, *51*, 6828–6838; *Angew. Chem.* **2012**, *124*, 6934–6944; d) K. L. Skubi, T. R. Blum, T. P. Yoon, *Chem. Rev.* **2016**, *116*, 10035–10074; e) X. Lang, J. Zhao, X. Chen, *Chem. Soc. Rev.* **2016**, *45*, 3026–3038; f) N. A. Romero, D. A. Nicewicz, *Chem. Rev.* **2016**, *116*, 10075–10166; g) M. H. Shaw, J. Twilton, D. W. C. MacMillan, *J. Org. Chem.* **2016**, *81*, 6898–6926; h) M. Parasram, V. Gevorgyan, *Chem. Soc. Rev.* **2017**, *46*, 6227–6240; i) K. N. Lee, M.-Y. Ngai, *Chem. Commun.* **2017**, *53*, 13093–13112; j) Y.-Q. Zou, F. M. Hoermann, T. Bach, *Chem. Soc. Rev.* **2018**, *47*, 278–290; k) C. B. Larsen, O. S. Wenger, *Chem. Eur. J.* **2018**, *24*, 2039–2058.
- [5] a) J. Twilton, C. Lee, P. Zhang, M. H. Shaw Evans, R. W. MacMillan, *Nat. Rev. Chem.* **2017**, *1*, 0052; b) K. L. Skubi, T. R. Blum, T. P. Yoon, *ACS Catal.* **2016**, *116*, 10035–10074; c) S. Reischauer, B. Pieber, *iScience* **2021**, *24*, 102209; d) C. Zhu, H. Yue, J. Jia, M. Rueping, *Angew. Chem. Int. Ed.* **2021**, *60*, 17810–17831; *Angew. Chem.* **2021**, *133*, 17954–17975; e) C. Zhu, H. Yue, L. Chu, M. Rueping, *Chem. Sci.* **2020**, *11*, 4051–4064.
- [6] a) L. Pitzer, J. L. Schwarz, F. Glorius, *Chem. Sci.* **2019**, *10*, 8285–8291; b) R. J. Wiles, G. A. Molander, *Isr. J. Org. Chem.* **2020**, *60*, 281–293.
- [7] For a photoredox methodology without metals, see: a) A. L. Berger, K. Donabauer, B. König, *Chem. Sci.* **2019**, *10*, 10991–10996; b) K. Donabauer, M. Maity, A. L. Berger, G. S. Huff, S. Crespi, B. König, *Chem. Sci.* **2019**, *10*, 5162–5166.
- [8] H.-M. Huang, P. Bellotti, F. Glorius, *Chem. Soc. Rev.* **2020**, *49*, 6186–6197.
- [9] a) J. L. Schwarz, F. Schäfers, A. Tlahuext-Aca, L. Lückemeier, F. Glorius, *J. Am. Chem. Soc.* **2018**, *140*, 12705–12709; b) F. Schäfers, L. Quach, L. J. Schwarz, M. Saladrigas, C. G. Daniliuc, F. Glorius, *ACS Catal.* **2020**, *10*, 11841–11847; c) L. J. Schwarz, H.-M. Huang, T. O. Paulisch, F. Glorius, *ACS Catal.* **2020**, *10*, 1621–1627; d) H.-M. Huang, P. Bellotti, C. Daniliuc, F. Glorius, *Angew. Chem. Int. Ed.* **2021**, *60*, 2464–2471; *Angew. Chem.* **2021**, *133*, 2494–2501; e) J. L. Schwarz, R. Kleinmans, T. O. Paulisch, F. Glorius, *J. Am. Chem. Soc.* **2020**, *142*, 2168–2174; f) H. Mitsunuma, S. Tanabe, H. Fuse, K. Ohkubo, M. Kanai, *Chem. Sci.* **2019**, *10*, 3459–3465; g) S. Tanabe, H. Mitsunuma, M. Kanai, *J. Am. Chem. Soc.* **2020**, *142*, 12374–12381; h) Y. Hirao, Y. Katayama, H. Mitsunuma, M. Kanai, *Org. Lett.* **2020**, *22*, 8584–8588; i) K. Yahata, S. Sakurai, S. Hori, S. Yoshioka, Y. Kaneko, K. Hasegawa, S. Akai, *Org. Lett.* **2020**, *22*, 1199–1203.
- [10] a) A. Gualandi, F. Calogero, M. Mazzarini, S. Guazzi, A. Fermi, G. Bergamini, P. G. Cozzi, *ACS Catal.* **2020**, *10*, 3857–3863; b) F. Calogero, A. Gualandi, S. Potenti, M. Di Matteo, A. Fermi, G. Bergamini, P. G. Cozzi, *J. Org. Chem.* **2021**, *86*, 7002–7009; c) F. Li, S. Lin, Y. Chen, C. Shi, H. Yan, C. Li, C. Wu, L. Lin, C. Duan, S. Shi, *Angew. Chem. Int. Ed.* **2021**, *60*, 1561–1566; *Angew. Chem.* **2021**, *133*, 1585–1590. For a review, see: d) A. Fermi, A. Gualandi, G. Bergamini, P. G. Cozzi, *Eur. J. Org. Chem.* **2020**, 6955–6965.
- [11] a) A. Gualandi, G. Rodeghiero, R. Perciaccante, T. P. Jansen, C. Moreno-Cabrero, C. Foucher, M. Marchini, P. Ceroni, P. G. Cozzi, *Adv. Synth. Catal.* **2021**, *363*, 1105–1111; b) A. Cristòfol, B. Limburg, A. W. Kleij, *Angew. Chem. Int. Ed.* **2021**, *60*, 15266–15270; *Angew. Chem.* **2021**, *133*, 15394–15398; c) C. Shi, F. Li, Y. Chen, S. Lin, E. Hao, Z. Guo, U. D. Tul Wosqa, L. Shi, *ACS Catal.* **2021**, *11*, 2992–2998; d) Y.-L. Li, S.-Q. Zhang, J. Chen, J.-B. Xia, *J. Am. Chem. Soc.* **2021**, *143*, 7306–7313.
- [12] S. Potenti, A. Gualandi, A. Puggioli, A. Fermi, G. Bergamini, P. G. Cozzi, *Eur. J. Org. Chem.* **2021**, 1624–1627.
- [13] U. B. Kim, D. J. Jung, H. J. Jeon, K. Rathwell, S.-G. Lee, *Chem. Rev.* **2020**, *120*, 13382–13433.
- [14] A. Gil, F. Albericio, M. Alvarez, *Chem. Rev.* **2017**, *117*, 8420–8446; and refs. therein.
- [15] A. Fürstner, N. Shi, *J. Am. Chem. Soc.* **1996**, *118*, 12349–12357.
- [16] G. C. Hargaden, P. J. Guiry, *Adv. Synth. Catal.* **2007**, *349*, 2407–2424.
- [17] For selected recent articles: a) N. Sugihara, K. Suzuki, Y. Nishimoto, M. Yasuda, *J. Am. Chem. Soc.* **2021**, *143*, 9308–9313; b) A. J. Bendel-Smith, S. C. Kim, M. Wasa, S. P. Roche,

- E. N. Jacobsen, *J. Am. Chem. Soc.* **2019**, *141*, 11414–11419; c) E. Le Grogne, J.-M. Chrétien, Z. Zammattio, J.-P. Quintard, *Chem. Rev.* **2015**, *115*, 10207–10260.
- [18] For selected recent articles: a) P. E. Hartmann, M. Lazzarotto, J. Pletz, S. Tanda, P. Neu, W. Goessler, W. Kroutil, A. D. Boese, M. Fuchs, *J. Org. Chem.* **2020**, *85*, 9672–9679; b) J. L. López-Martínez, I. Torres-García, I. Rodríguez-García, M. Muñoz-Dorado, M. Álvarez Corral, *J. Org. Chem.* **2019**, *84*, 806–816.
- [19] For selected recent articles: a) S. W. Kim, C. C. Meyer, B. K. Mai, P. Liu, M. J. Krische, *ACS Catal.* **2019**, *9*, 9158–9163; b) J. M. Cabrera, J. Tauber, W. Zhang, M. Xiang, M. J. Krische, *J. Am. Chem. Soc.* **2018**, *140*, 9392–9395; c) S. W. Kim, T. W. Gilmar, A. Brito, W.-O. Jung, J. R. Zbieg, C. E. Stivala, M. J. Krische, *J. Am. Chem. Soc.* **2018**, *140*, 9087–9090.
- [20] For selected recent articles: a) S. Umemiya, M. Terada, *Org. Lett.* **2021**, *23*, 3767–3771; b) E. Wheatley, J. M. Zanghi, S. J. Meek, *Org. Lett.* **2020**, *22*, 9269–9275.
- [21] a) E. Ronchi, S. M. Paradine, E. N. Jacobsen, *J. Am. Chem. Soc.* **2021**, *143*, 7272–7278; b) H. Zhou, H. Y. Bae, M. Leutzsch, J. L. Kennemur, D. Bécart, B. List, *J. Am. Chem. Soc.* **2020**, *142*, 13695–13700.
- [22] a) H. Mayr, G. Hagen, *J. Chem. Soc. Chem. Commun.* **1989**, 91–92.
- [23] a) A. Gualandi, G. Rodeghiero, A. Faraone, F. Patuzzo, M. Marchini, F. Calogero, R. Perciaccante, T. P. Jansen, P. Ceroni, P. G. Cozzi, *Chem. Commun.* **2019**, *55*, 6838–6841. For a photoredox nickel-mediated crotylation of aldehydes, see: b) Y.-L. Li, W.-D. Li, Z.-Y. Gu, J. Chen, J.-B. Xia, *ACS Catal.* **2020**, *10*, 1528–1534.
- [24] For a nickel-mediated enantioselective allylation of aldehydes, with allylcarbonates, in the presence of stoichiometric amount of zinc, see: Z. Tan, X. Wan, Z. Zang, Q. Qia, W. Deng, H. Gong, *Chem. Commun.* **2014**, *50*, 3827–3831. However, addition of simple allylcarbonate with the methodology gave max 66% e.e. in a single example, and by using Ni(COD)₂ (10 mol %) in the presence of copper salt as additive.
- [25] a) E. Speckmeier, T. G. Fischer, K. Zeitler, *J. Am. Chem. Soc.* **2018**, *140*, 15353–15356. For pioneering studies of TADF dyes in photoredox catalysis: b) J. Luo, J. Zhang, *ACS Catal.* **2016**, *6*, 873–877. For recent reviews, see: c) T.-Y. Shang, L.-H. Lu, Z. Cao, Y. Liu, W.-M. He, B. Yu, *Chem. Commun.* **2019**, *55*, 5408–5419; d) A. Gualandi, M. Anselmi, F. Calogero, S. Potenti, E. Bassan, P. Ceroni, P. G. Cozzi, *Org. Biomol. Chem.* **2021**, *19*, 3527–3550.
- [26] a) C. Prentice, J. Morrisson, A. D. Smith, E. Zysman-Colman, *Beilstein J. Org. Chem.* **2020**, *16*, 2363–2441; b) D. Saha, *Chem. Asian J.* **2020**, *15*, 2129–2152; c) B.-C. Hong, *Org. Biomol. Chem.* **2020**, *18*, 4298–4353; d) A. Lipp, S. O. Badir, G. A. Molander, *Angew. Chem. Int. Ed.* **2021**, *60*, 1714–1726; *Angew. Chem.* **2021**, *133*, 1738–1750.
- [27] a) L. Hofstra, T. J. DeLano, S. E. Reisman, *Org. Synth.* **2020**, *97*, 172–188. For a recent review of oxazolines ligand in asymmetric catalysis, see: b) R. Connon, B. Roche, B. V. Rokade, P. J. Guiry, *Chem. Rev.* **2021**, *121*, 6373–6521.
- [28] C.-H. Lim, M. Kudisch, B. Liu, G. M. Miyake, *J. Am. Chem. Soc.* **2018**, *140*, 7667–7673.
- [29] a) Y. Im, J. Yeob Lee, *J. Inf. Disp.* **2017**, *18*, 101–117; b) W. Che, X. Xie, Z. Li, *Asian J. Org. Chem.* **2020**, *9*, 1262–1276.
- [30] D. A. Evans, K. A. Woerpel, M. J. Scott, *Angew. Chem. Int. Ed. Engl.* **1992**, *31*, 430–432; *Angew. Chem.* **1992**, *104*, 439–441.
- [31] S. Prévost, K. Thai, N. Schützenmeister, G. Coulthard, W. Erb, V. K. Aggarwal, *Org. Lett.* **2015**, *17*, 504–507.
- [32] J. Chen, D. Liu, D. Fan, Y. Liu, W. Zhang, *Tetrahedron* **2013**, *69*, 8161–8168.
- [33] B. Maity, C. Zhu, H. Yue, L. Huang, M. Harb, Y. Minenkov, M. Rueping, L. Cavallo, *J. Am. Chem. Soc.* **2020**, *142*, 16942–16952.
- [34] a) L. Falivene, R. Credendino, A. Poater, A. Petta, L. Serra, R. Oliva, V. Scarano, L. Cavallo, *Organometallics* **2016**, *35*, 2286–2293; b) L. Falivene, Z. Cao, A. Petta, L. Serra, A. Poater, R. Oliva, V. Scarano, L. Cavallo, *Nat. Chem.* **2019**, *11*, 872–879; c) B. Maity, C. Zhu, M. Rueping, L. Cavallo, *ACS Catal.* **2021**, *11*, 13973–13982.

Manuscript received: November 4, 2021

Accepted manuscript online: December 22, 2021

Version of record online: January 24, 2022